

Article

Preparation of V₂O₅ Thin Film by Sol–Gel Technique and Pen Plotter Printing

Philipp Yu. Gorobtsov *, Tatiana L. Simonenko , Nikolay P. Simonenko *, Elizaveta P. Simonenko 
and Nikolay T. Kuznetsov

Kurnakov Institute of General and Inorganic Chemistry of the Russian Academy of Sciences, 31 Leninsky pr., Moscow 119991, Russia

* Correspondence: phigoros@gmail.com (P.Y.G.); n_simonenko@mail.ru (N.P.S.)

Abstract: The work is dedicated to study of thin V₂O₅ film formation by pen plotter printing using vanadyl alkoxyacetylacetonate as hydrolytically active precursor. Solution of the prepared vanadyl butoxyacetylacetonate complex with 87% of butoxyl groups was used as functional ink for pen plotter printing of thin V₂O₅ film on surface of specialized chip. According to atomic force microscopy (AFM) and scanning electron microscopy (SEM), oxide film consists of nanorods 35–75 nm in thickness and 120–285 nm in length, with crystallite size of 54 ± 4 nm. Data from Rietveld refinement of the X-ray powder diffraction results and work function value (4.54 eV) indicate high content of defects (such as oxygen vacancies) in the material. Electrophysical properties study suggests that correlated barrier hopping of the charge carriers is the main conductivity mechanism. Conductivity activation energy E_a was found to be 0.24 eV.

Keywords: V₂O₅; thin film; pen plotter printing; sol-gel synthesis; alkoxyacetylacetonate



Citation: Gorobtsov, P.Y.; Simonenko, T.L.; Simonenko, N.P.; Simonenko, E.P.; Kuznetsov, N.T. Preparation of V₂O₅ Thin Film by Sol–Gel Technique and Pen Plotter Printing. *Colloids Interfaces* **2023**, *7*, 20. <https://doi.org/10.3390/colloids7010020>

Received: 31 January 2023

Revised: 5 March 2023

Accepted: 11 March 2023

Published: 15 March 2023



Copyright: © 2023 by the authors. Licensee MDPI, Basel, Switzerland. This article is an open access article distributed under the terms and conditions of the Creative Commons Attribution (CC BY) license (<https://creativecommons.org/licenses/by/4.0/>).

1. Introduction

Vanadium oxide-based thin films have recently been investigated for a variety of applications. For example, V₂O₅-based coatings are promising as electrochromic layers [1–4] due to their ability to change color from almost transparent yellow to dark green and dark blue when reduced, or to orange when oxidized on an anode [4,5], as well as their high capacity for lithium ion intercalation [3]. Due to the latter property, as well as high specific capacitance, cycling stability, and good kinetic characteristics upon ion intercalation, vanadium(V)-based thin films are promising cathode materials in lithium-ion batteries [6,7] and supercapacitors [8–10]. V₂O₅ thin films are also of great interest as components for solar cells and LEDs [11–14]. In addition, vanadium pentoxide coatings can demonstrate high selectivity and chemosensory response in the detection of nitrogen dioxide [15], ammonia [16] and various organic compounds [17–19].

At the same time, it is known that the properties of any material, including thin films, depend not only on its elemental or phase composition, but also on the preparation technique. For example, the technique and conditions of synthesis affect the microstructure of the material and amount of defects (such as oxygen vacancies) in it. Chemical precipitation [20,21], hydrothermal techniques [22,23] and various sol-gel technology modifications [24] are often used for V₂O₅ synthesis. Each of these has its own advantages, but the sol-gel technology from our point of view is one of the most variable both in terms of synthesis parameter control and in terms of possible combination with various techniques of thin film deposition. At the same time, the most widely encountered modifications in the literature regarding sol–gel technology for the preparation of vanadium pentoxide are the approaches utilizing vanadium acid condensation and the hydrolysis of vanadium(V) oxytriisopropoxide [24–28]. However, techniques based on the reaction of V₂O₅ with H₂O₂ or preparation of V₂O₅ sols by passing vanadate solutions through cation-exchange resins have a disadvantage of low control over the chemical process of oxide

preparation. Consequently, these techniques are deprived of one of the main advantages of the classic sol-gel technology, namely, the ability to influence the microstructure of the resulting material at the initial stage of the formation of solid phase particles. The classical sol-gel approach, based on the hydrolysis of alkoxides, is much more flexible in this respect, since it allows one to control the hydrolysis and polycondensation processes by adding acidic or basic catalysts (for example, acetic acid, as in [25]), changing the composition of the hydrolytically active precursor. However, the latter approach is very rarely used to obtain V_2O_5 , although it can, for example, eliminate such drawbacks as excessively rapid hydrolysis. In this regard, we consider it promising to use metal acetylacetonates with partial substitution of chelate ligands for alkoxy fragments as precursors for sol-gel synthesis of vanadium(V) oxide [29,30]. Besides, for practical applications of vanadium pentoxide, the content of vanadium in other oxidative states is an important factor, since it affects the properties of the resulting material. For some applications, the presence of significant amounts of vanadium(IV) is a positive factor [31,32]. Therefore, solutions containing vanadium(IV) may be promising as a precursor for preparation of V_2O_5 , when vanadium dioxide formed at the first stage is oxidized to pentoxide after additional heat treatment in the air, preserving a certain concentration of vanadium(IV) ions.

As already mentioned, sol-gel technology is compatible with a wide range of thin film deposition techniques. For example, it is often combined with spin-coating and dip-coating [25,29]. Recently, however, more and more attention in the field of film deposition has been paid to printing technologies, such as ink-jet printing [28,33,34], microextrusion printing [35,36] or pen plotter printing [30,37,38]. These processes provide high reproducibility of the microstructural and functional characteristics of the films and simplify the production of multicomponent coatings, including those with complicated geometries. In addition to these, pen plotter printing has other advantages, such as affordability, availability of consumable materials, possibility of printing on surfaces of different texture and roughness, absence of strict requirements regarding the rheological properties of the so-called functional inks, and convenience of coating using precursor solutions for sol-gel synthesis of various nanomaterials. The pen plotter printing process can be described as follows. First, a pen, often stuffed inside with a special foamy ink absorber, is filled with functional ink. Then, the filled pen is put into a special holder on a plotter, which moves along the X and Y planes, normally without controlled movement on the Z axis, so this technique is only applicable to film preparation [39].

Thus, in this work we investigate the process of pen plotter printing of V_2O_5 thin films combined with sol-gel technology based on the use of hydrolytically active heteroligand complexes of the composition $[VO(C_5H_7O_2)_{2-x}(C_4H_9O)_x]$ as precursors.

2. Materials and Methods

2.1. Materials

The reagents used in the study were as follows: n-butanol (C_4H_9OH , 99%, Ekos-1, Moscow, Russia) for complex solution preparation, vanadyl acetylacetonate ($[VO(C_5H_7O_2)_2]$, 98%, Sigma-Aldrich, St. Louis, MO, USA) as starting reagent for heteroligand complex preparation.

2.2. Hydrolytically Active Precursor Synthesis

Heteroligand complexes of the composition $[VO(C_5H_7O_2)_{2-x}(C_4H_9O)_x]$ were used as the vanadium oxide precursors. They were prepared by heat treatment of a solution of vanadyl acetylacetonate $[VO(C_5H_7O_2)_2]$ in n-butanol. Heat treatment lasted 18 h, with the temperature of the oil bath (in which the flask with the solution and reflux condenser were immersed) being 140 °C. The formation of the alkoxoacetylacetonate complex was confirmed by infrared spectroscopy and UV-spectrophotometry.

2.3. Pen Plotter Printing of Oxide Films

The solution of the synthesized complex was further used as a functional ink in the application of V_2O_5 films by pen plotter printing. The scheme of the process is shown

in Figure 1. A specialized Pt/Al₂O₃/Pt (further PAP) chip was used as a substrate for subsequent measurement of electrophysical properties. The chip which is an α -Al₂O₃ substrate ($R_a = 100$ nm) with platinum counter-pin electrodes on the front side and a platinum meander microheater on the back side. The solution film was applied to the front side of the chip in the area of the platinum counter-pin electrodes. The printing speed was 50 mm/min, the distance between the lines in the digital model was 100 μ m. As a result, a 5-layer film was formed. After applying each layer, the sample was heat-treated in air at 200 °C for 10 min. After all layers had been applied, the sample was further heat-treated in air at 300 °C for 1 h to remove organic components and oxidize the material to V₂O₅. Similarly, a vanadium(V) oxide film was obtained on a glass substrate to clarify its crystal structure.

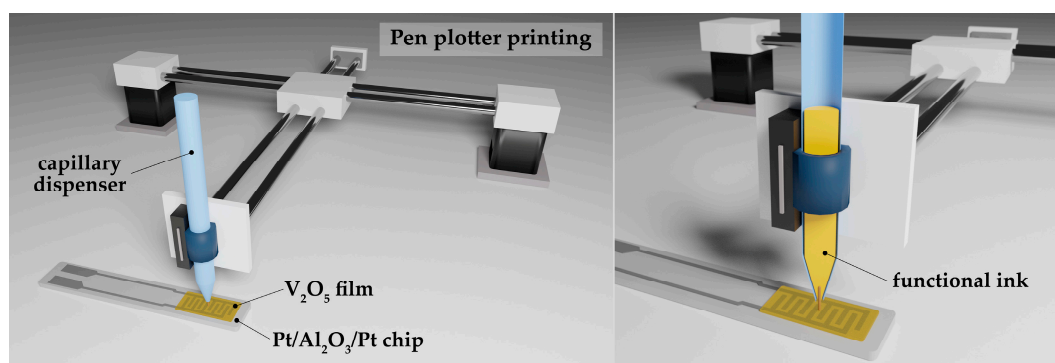


Figure 1. Scheme of V₂O₅ thin film pen plotter printing process.

2.4. Instrumentation

An InfraLUM FT-08 infrared spectrometer (Lumex, St. Petersburg, Russia) was used to record vibrational spectra (IR spectra) of the complex solution. The spectra were recorded in the range of 350–2000 cm⁻¹.

SF-56 spectrophotometer (OKB Spectr, St. Petersburg, Russia) was used to record UV spectra. Spectra were recorded in the wavelength range of 250–325 nm for solutions diluted to a complex concentration of 2–10⁻⁴ mol/L.

X-ray powder diffraction (XRD) of the deposited films was performed with a D8-Advance diffractometer (Bruker, Billerica, MA, USA; CuK $\alpha = 1.5418$ Å, Ni filter, E = 40 keV, I = 40 mA, range 2 θ 5–80°, signal accumulation time 0.3 s/point, resolution 0.02°).

The microstructure of V₂O₅ films was studied by scanning electron microscopy (SEM, NVision 40 dual-beam workstation, Carl Zeiss, Inc., Jena, Germany).

The printed V₂O₅ coatings were also examined by atomic force microscopy (AFM) on the NT-MDT Solver PRO (NT-MDT, Zelenograd, Russia). Both surface morphology and local electrophysical properties of the material were characterized. For the latter, the techniques of Kelvin Probe Force Microscopy (KPFM), Scanning Capacitive Microscopy (SCM), and Scanning Spreading Resistance Microscopy (SSRM) were used. Scanning in all techniques, except SSRM, was performed in the semicontact mode; ETALON HA_HR probes (ScanSens, Bremen, Germany) with W₂C conductive coating (tip curvature radius ≤ 35 nm) were used. Within the framework of the KPFM, the value of the electron work function φ_{oxide} for the surface of the oxide film was measured. For this purpose, the surface was scanned five times with a probe with a predetermined work function φ_{tip} , then the average value of the contact potential φ_{cpd} was determined for each scan. The value of φ_{oxide} was then calculated as the difference between φ_{tip} and φ_{cpd} . The scanning with SSRM technique was performed in contact mode. Voltage was applied to the sample through a metal clamp in contact with the platinum electrode of the PAP substrate.

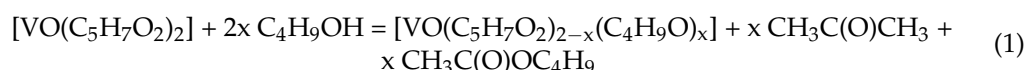
The electrical conductivity of the film printed on the surface of the Pt/Al₂O₃/Pt chip was measured by impedance spectroscopy in the temperature range 50–300 °C and frequency range 1 MHz–0.4 Hz using a potentiostat-galvanostat equipped with an electrochemical

impedance measurement module (P-45X, Electrochemical Instruments, Chernogolovka, Russia). The chip was heated by applying voltage to the contacts of the meander microheater using a power supply (QJE, PS3003, Ningbo JiuYuan Electronic, Ningbo, China), and temperature control was performed using a Testo 868 thermal imager (Testo, Lenzkirch, Germany).

3. Results and Discussion

3.1. Precursor Synthesis and Characterization

The synthesis of $[\text{VO}(\text{C}_5\text{H}_7\text{O}_2)_{2-x}(\text{C}_4\text{H}_9\text{O})_x]$ complexes proceeds with partial destructive substitution of chelate ligands during the heat treatment of vanadyl acetylacetonate in n-butyl alcohol according to the following reaction equation:



The progress of the synthesis carried out in this way can be monitored by spectral means, namely UV spectrophotometry and infrared spectroscopy. Thus, two absorption bands in the wavelength range of 250–320 nm are observed in the obtained UV spectra of the heteroligand complexes solution (Figure 2). The maximum of the first band is near 273 nm, and the maximum of the second is at ~308 nm. The first of these bands probably refers to the free acetylacetonate, which may be present in the reaction system. The second band refers to the coordinated $\text{C}_5\text{H}_7\text{O}_2$ ligand. It can be seen that the intensity of both bands significantly decreased as a result of the heat treatment, which confirms the occurrence of the reaction with partial destruction of the acetylacetonate ligand (and the free acetylacetonate impurity). Based on the spectral data obtained, we can quantitatively determine the degree to which the process of destructive substitution of chelate ligands proceeds by calculating the fraction of butoxy groups in the complex according to the following formula:

$$\alpha = (1 - D'_{308}/D_{308}) \cdot 100\%, \quad (2)$$

with α —fraction of butoxy groups in the complex, D'_{308} —optical density of solution at 308 nm after heat treatment, D_{308} —optical density of original solution at 308 nm. Taking the baseline into account, the α value after 18 h of heat treatment was about 87%. This content of alkoxy groups in the composition of the complex should significantly increase its hydrolytic activity.

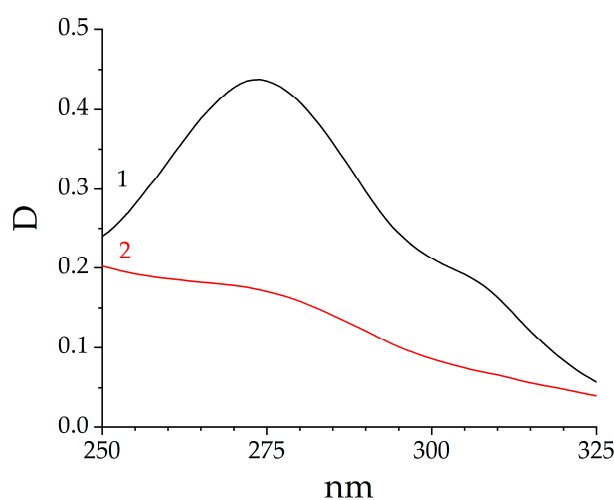


Figure 2. UV spectra of the acetylacetonate solution (1) and the vanadyl alkoxoacetylacetonate solution (2) prepared as a result of its heat treatment for 18 h.

The results of IR spectroscopy (Figure 3) confirm the conclusions drawn from the analysis of the electron spectra. Thus, absorption bands with maxima at 1522 and 1560 cm^{-1} ,

characteristic for vibrations of the C=O and C=C groups in the coordinated acetylacetonate ligands, observed on the spectrum of vanadyl acetylacetonate, are absent on the spectrum of the complex solution after its heat treatment. At the same time, an absorption band appears with two maxima (at 1743 and 1720 cm^{-1}) related to vibrations of the carboxyl group C=O in the products of chelate ligand destruction (acetone and butyl acetate). There are also a few other differences between two spectra, such as slight change in the shape of absorption bands situated in the regions of $\sim 1300\text{--}1500\text{ cm}^{-1}$, $900\text{--}1100\text{ cm}^{-1}$, and also varying intensity of the bands in these regions. Slight changes in shape can be attributed to the changes in complex geometry and structure due to chelate ligand substitution with butoxyl species, while intensity in these regions might be different due to a slightly different size of aliquot taken for IR spectroscopy.

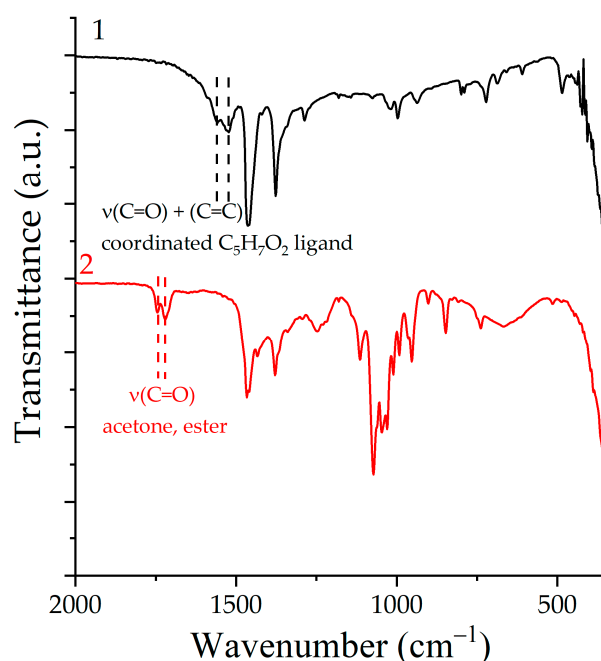


Figure 3. IR spectra of acetylacetonate solution (1) and the vanadyl alkoxoacetylacetonate solution (2) obtained as a result of its heat treatment for 18 h.

3.2. V_2O_5 Thin Film Crystal Structure

X-ray powder diffraction analysis (XRD) was used to study the crystal structure of the oxide film obtained as a result of heat treatment (Figure 4). As can be seen from the diffractogram for the oxide film deposited on a glass substrate, the reflexes present agree well with the ICSD card #41030 for orthorhombic V_2O_5 and confirm that the chosen regime of heat treatment of the material leads to its crystallization and oxidation into vanadium pentaoxide. A full-profile analysis of this diffractogram was also performed, resulting in the calculation of the average size of crystallites and lattice parameters. Thus, the average crystallite size in this case was $54 \pm 4\text{ nm}$, and the lattice parameters have the following values: $a = 11.502(3)\text{ \AA}$, $b = 3.559(1)\text{ \AA}$, $c = 4.388(2)\text{ \AA}$, the cell volume was 179.61 \AA^3 . When comparing the results with the literature data ($a = 11.512\text{ \AA}$, $b = 3.564\text{ \AA}$, $c = 4.368\text{ \AA}$) [40,41], it can be noticed that in our case the cell is somewhat compressed by parameters a and b and expanded by parameter c . Due to the fact that the average crystallite size reaches a relatively large value, the degree of crystallinity of the material is quite high, respectively, the differences in the cell parameters are probably not due to the incomplete crystallization process. Consequently, they can be explained by the peculiarities of the structure and composition of the oxide, i.e., the presence of defects. It can be assumed that the obtained material has an increased concentration of oxygen vacancies, which leads to a decrease in parameters a and b . The increase in the parameter c is also presumably due to the high

content of oxygen vacancies: the parameter c is related to the distance between the layers in the crystal structure of the oxide, and the layers are linked by the interaction between the oxygen at the top of the pyramidal structure surrounding the vanadium in one layer and vanadium from the neighboring layer [42].

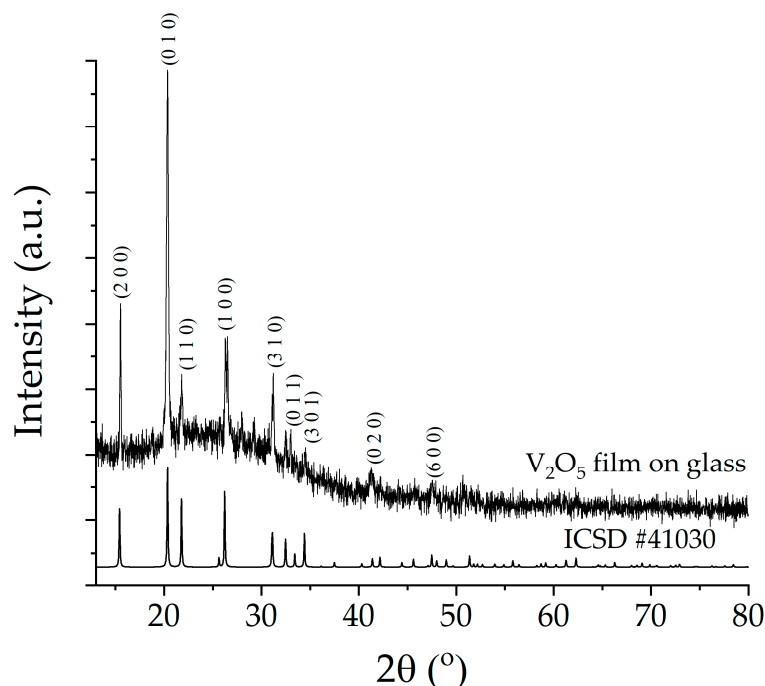


Figure 4. Diffractogram of the obtained V_2O_5 film on a glass substrate.

3.3. Oxide Film Microstructure

SEM study of the microstructure of the oxide film on the PAP surface showed (Figure 5) that the film, although not completely covering the substrate area (which can be seen from presence of bare alumina grains of $\sim 1 \mu\text{m}$ size), is continuous and formed by well-defined, elongated nanorods. Furthermore, some V_2O_5 particles are combined into agglomerates, fused by their lateral facets. Agglomeration and fusion of the nanorods is most likely caused by the heat treatment at 300°C . The average length of the rods is $259 \pm 25 \text{ nm}$ and the width is $68 \pm 6 \text{ nm}$. Comparison of the particle size observed by SEM with the average crystallite size determined by XRD suggests that the oxide nanorods are mostly composed of several crystallites.

The SEM data for the oxide film are basically confirmed by the AFM results (Figure 6). The topographic image of the oxide film surface (Figure 6a) and the phase contrast scan results (Figure 6b) also demonstrate that the material consists of nanorods $130 \pm 13 \text{ nm}$ long and $39 \pm 3 \text{ nm}$ wide (measurements based on phase contrast images), with thickness (from topography scans) of $23 \pm 5 \text{ nm}$. Also, the AFM results show that the surface roughness of the oxide film has a smaller value (in the area of $342 \mu\text{m}^2$ the R_a value is $68 \pm 6 \text{ nm}$) compared to the pure Al_2O_3 substrate ($R_a = 100 \pm 5 \text{ nm}$). Mapping of the surface potential distribution during KPFM (Figure 6c) showed that the film, despite its relatively low density, has a sufficiently high conductivity: the potential value is evenly distributed across the film surface (the maximum difference in the surface potential is $\sim 15 \text{ mV}$). It can also be noted that a higher value of the contact potential difference corresponds to higher areas of the studied material, although the opposite is often observed for oxide semiconductor materials. The results of the capacitance gradient mapping for “probe tip-sample micro-region” capacitor (Figure 6d), obtained as a result of SCM, show a larger gradient (lighter areas) at the inter-particle boundaries, which indicates the preferential nature of inter-grain conductivity in the material.

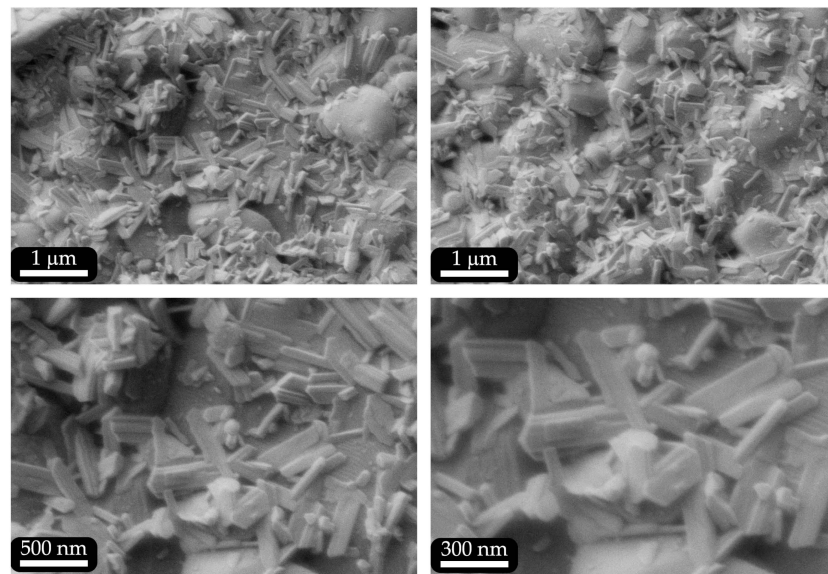


Figure 5. Microstructure of the V_2O_5 film printed on the PAP surface (according to SEM data).

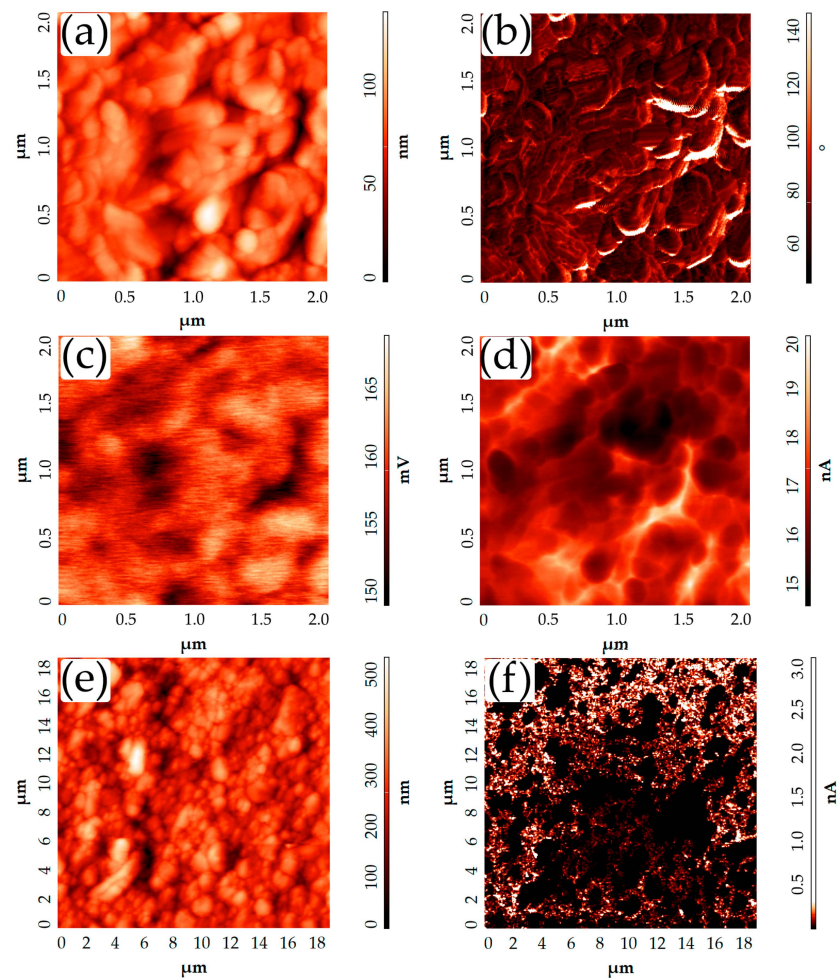


Figure 6. Results of AFM of V_2O_5 film on PAP: topography in the semicontact mode (a), image in the phase contrast mode (b), surface potential distribution map (KPFM) (c), capacitor tip-sample microregion capacitance gradient distribution map (SCM) (d), topography during SSRM recording (e), current distribution between probe and sample (3 V bias voltage) (SSRM) (f).

The results of scanning spreading resistance microscopy (SSRM) (Figure 6e,f) further demonstrate the contact between the V_2O_5 particles over the entire area of the film: the bright areas in the image correspond to the areas where the current passes between the probe and the sample.

The value of the electron work function of the printed film, 4.54 ± 0.01 eV, was also calculated on the basis of the KPFM results. This value is outside the interval of 4.7–5.3 eV, in which, as a rule, the value for work function of V_2O_5 is observed. [25,43–45]. In particular, this is lower than the values for other vanadium(V) oxide-based materials obtained by us from similar precursors: 4.89 eV in the case of thin film deposition by dip-coating in alkoxyacetylacetonate solution [29] and 4.81 eV in the case of thick film deposition by microextrusion printing with the use of vanadium oxide powder obtained during hydrothermal treatment of the dispersed system resulting from the precursor hydrolysis [35]. This result indicates a significantly increased defectiveness of the V_2O_5 film obtained in the current study, which also agrees with the results of the full-profile analysis of the corresponding diffractogram.

3.4. Electrophysical Properties of Prepared V_2O_5 Film

Figure 7 shows frequency dependences of conductivity of V_2O_5 film under study on alternating current in the temperature range of 50–300 °C. They are characterized by a plateau (from 1 to 104 Hz) that does not depend on frequency and is caused by diffusion of charge carriers (ions) in the material arising when alternating current is applied to it. At higher frequencies, there is the so-called dispersion region, characterized by an increase in conductivity due to hopping of carriers. As can be seen from the above figure, the dispersion region gradually shifts to a higher frequency range with increasing temperature, while there is also an increase in the AC conductivity value (σ_{ac}), which is typical for materials of similar composition and semiconductors in general [46].

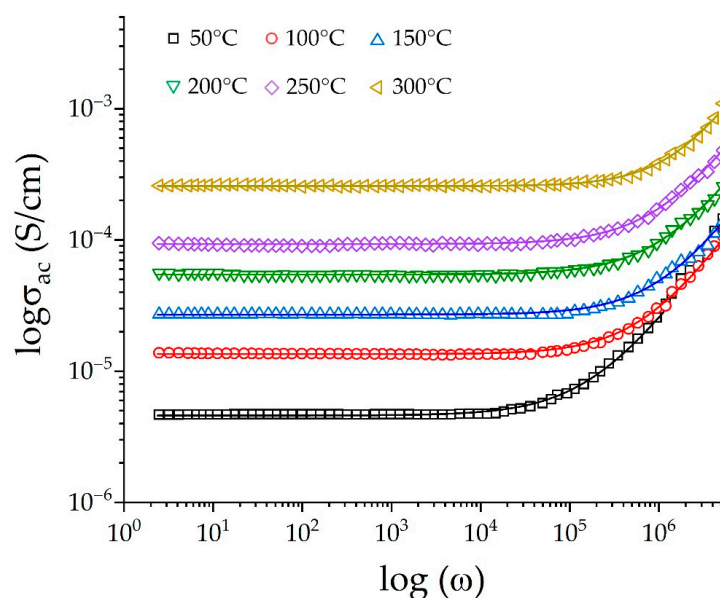


Figure 7. Frequency dependences of AC conductivity in the temperature range 50–300 °C.

The dependence of the conductivity of the studied film on frequency and temperature is well described by the Jonscher power law (3):

$$\sigma_{ac}(\omega, T) = \sigma_{dc}(T) + A\omega^s, \quad (3)$$

where σ_{ac} is the value of total conductivity measured at alternating current, σ_{dc} is the conductivity at direct current, ω is the angular frequency of the applied electric current, and the parameters A and s are fitting factors determined by the nature of the material

under study and dependent on temperature and frequency. The value of s determines the type of motion (translational or localized) of the charge carriers. It is assumed that if $s < 1$, the motion is translational, and if $s > 1$, the motion is localized. Analyzing the temperature dependence of the index s , it is possible to assume different mechanisms of jump conductivity [47]. In our case, the value of s decreases from 1 to 0.8 when the temperature increases from 50 to 300 °C, which further indicates a hopping mechanism of conductivity according to the correlated barrier hopping model in the case of AC conductivity. This model assumes unipolar or bipolar jumps of charge carriers over the Coulomb barrier W_M separating the two defect centers, and predicts a decrease in the value of the parameter s as the temperature increases.

The σ_{dc} values calculated using Jonscher's law were further used to construct the temperature dependence of conductivity, as well as to calculate its activation energy using the Arrhenius Equation (4):

$$\sigma_{dc} = \sigma_0 \cdot \exp(-E_a/k_B T), \quad (4)$$

where σ_0 , k_B , E_a are the pre-exponential factor, Boltzmann constant, and conductivity activation energy, respectively. It can be seen that σ_{dc} increases with temperature, which is a characteristic behavior of the semiconductor and confirms the thermoactivated conduction mechanism in the studied sample (Figure 8a). Using the graph of the temperature dependence of conductivity in Arrhenius coordinates (Figure 8b) and Equation (2), the value of film activation energy was estimated at 0.24 eV, which is in good agreement with the values of E_a for materials of similar composition [46]. Nevertheless, the electrical conductivity values obtained in our study are inferior to those for vanadium pentoxide-based planar materials described in the literature [48,49]. This fact may be due to the lower density of the printed coating, which reduces the contact area between the grains, increasing the resistance of the material.

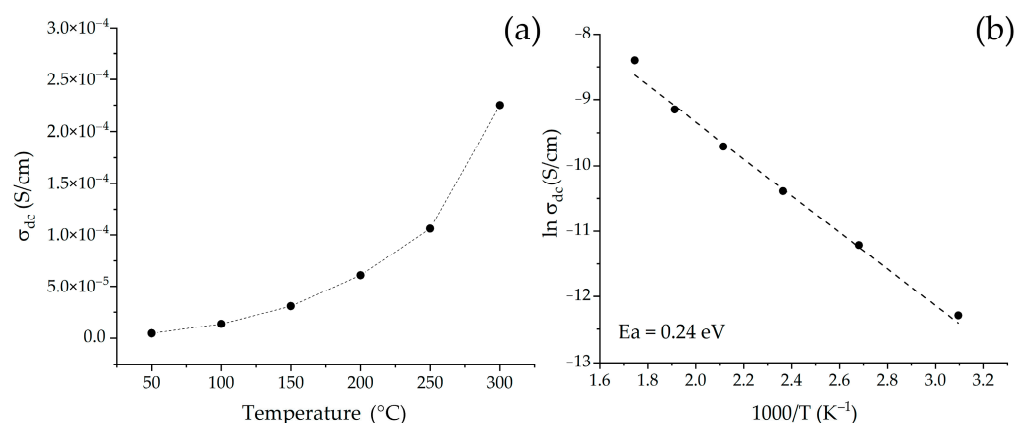


Figure 8. Temperature dependence of σ_{dc} (a) and $\ln \sigma_{dc}$ of the studied sample (b).

4. Conclusions

As a result of the research, the process of V_2O_5 thin film formation by combining sol-gel technology and pen plotter printing was studied. A homogenous solution of synthesized hydrolytically active alkoxoacetylacetonate $[VO(C_5H_7O_2)_{2-x}(C_4H_9O)_x]$ was used as a functional ink. This approach made it possible to obtain thin films composed of vanadium(V) oxide, formed by nanorods with dimensions of 120–285 nm in length and 35–75 nm in width. The film has an activation energy of conductivity $E_a = 0.24$ eV, which agrees well with the literature data, and demonstrates the hopping character of conductivity. In addition, when studying the material by the SSRM method, it is further evident that the film conducts current rather well: in some areas the current between the probe and the sample reaches up to 2–3 nA. XRD results showed that the obtained V_2O_5 film is characterized by an orthorhombic crystal lattice, and compared with the literature data, there is a slight decrease in parameters a and b with a simultaneous increase in

parameter c , which may indicate a high number of defects, in particular, oxygen vacancies, in the film composition. This hypothesis is confirmed by the low value of the electron work function for the material surface (4.54 eV), calculated using KPFM data. The results obtained confirm the promising application of the pen plotter printing technique combined with sol-gel technology based on the use of alkoxoacetylacetonate vanadyl as precursor for the preparation of V_2O_5 thin films for various purposes, including such as electrochromic devices, alternative energy devices, and resistive gas sensors

Author Contributions: Conceptualization, N.P.S. and P.Y.G.; investigation, P.Y.G., T.L.S. and N.P.S.; writing—original draft preparation, P.Y.G., T.L.S. and N.P.S.; writing—review and editing, N.P.S.; visualization, P.Y.G. and T.L.S.; supervision, N.P.S., E.P.S. and N.T.K. All authors have read and agreed to the published version of the manuscript.

Funding: The synthesis of the studied nanomaterials was funded by Russian Foundation for Basic Research, project no. 20-33-90136. The SEM and X-ray powder diffraction analyses was performed using shared experimental facilities supported by IGIC RAS state assignment.

Institutional Review Board Statement: Not applicable.

Informed Consent Statement: Not applicable.

Data Availability Statement: Not applicable.

Conflicts of Interest: The authors declare no conflict of interest.

References

1. Cheng, K.C.; Chen, F.R.; Kai, J.J. V_2O_5 Nanowires as a Functional Material for Electrochromic Device. *Sol. Energy Mater. Sol. Cells* **2006**, *90*, 1156–1165. [[CrossRef](#)]
2. Wang, Y.; Cao, G. Li^+ -Intercalation Electrochemical/Electrochromic Properties of Vanadium Pentoxide Films by Sol Electrophoretic Deposition. *Electrochim. Acta* **2006**, *51*, 4865–4872. [[CrossRef](#)]
3. Ramana, C.V.; Smith, R.J.; Hussain, O.M.; Chusuei, C.C.; Julien, C.M. Correlation between Growth Conditions, Microstructure, and Optical Properties in Pulsed-Laser-Deposited V_2O_5 Thin Films. *Chem. Mater.* **2005**, *17*, 1213–1219. [[CrossRef](#)]
4. Jin, A.; Chen, W.; Zhu, Q.; Jian, Z. Multi-Electrochromism Behavior and Electrochromic Mechanism of Electrodeposited Molybdenum Doped Vanadium Pentoxide Films. *Electrochim. Acta* **2010**, *55*, 6408–6414. [[CrossRef](#)]
5. Zanarini, S.; di Lupo, F.; Bedini, A.; Vankova, S.; Garino, N.; Francia, C.; Bodoardo, S. Three-Colored Electrochromic Lithiated Vanadium Oxides: The Role of Surface Superoxides in the Electro-Generation of the Red State. *J. Mater. Chem. C Mater.* **2014**, *2*, 8854–8857. [[CrossRef](#)]
6. Wang, S.; Li, S.; Sun, Y.; Feng, X.; Chen, C. Three-Dimensional Porous V_2O_5 Cathode with Ultra High Rate Capability. *Energy Environ. Sci.* **2011**, *4*, 2854–2857. [[CrossRef](#)]
7. Liu, Y.; Clark, M.; Zhang, Q.; Yu, D.; Liu, D.; Liu, J.; Cao, G. V_2O_5 Nano-Electrodes with High Power and Energy Densities for Thin Film Li-Ion Batteries. *Adv. Energy Mater.* **2011**, *1*, 194–202. [[CrossRef](#)]
8. Narayanan, R. Single Step Hydrothermal Synthesis of Carbon Nanodot Decorated V_2O_5 Nanobelts as Hybrid Conducting Material for Supercapacitor Application. *J. Solid State Chem.* **2017**, *253*, 103–112. [[CrossRef](#)]
9. Jeyalakshmi, K.; Vijayakumar, S.; Nagamuthu, S.; Muralidharan, G. Effect of Annealing Temperature on the Supercapacitor Behaviour of β - V_2O_5 Thin Films. *Mater. Res. Bull.* **2013**, *48*, 760–766. [[CrossRef](#)]
10. De Freitas Neto, D.B.; Parmar, R.; Matsubara, E.Y.; Minicucci, M.; Gunnella, R.; Rosolen, J.M. Nanostructured V_2O_5 .NH₂O/Cup-Stacked Carbon Nanotube Composite with Remarkable Li^+ Specific Capacity. *Solid State Ion.* **2021**, *363*, 115590. [[CrossRef](#)]
11. Zhang, L.; Jiang, C.; Wu, C.; Ju, H.; Jiang, G.; Liu, W.; Zhu, C.; Chen, T. V_2O_5 as Hole Transporting Material for Efficient All Inorganic Sb_2S_3 Solar Cells. *ACS Appl. Mater. Interfaces* **2018**, *10*, 27098–27105. [[CrossRef](#)]
12. Zilberberg, K.; Trost, S.; Schmidt, H.; Riedl, T. Solution Processed Vanadium Pentoxide as Charge Extraction Layer for Organic Solar Cells. *Adv. Energy Mater.* **2011**, *1*, 377–381. [[CrossRef](#)]
13. Wang, D.; Elumalai, N.K.; Mahmud, M.A.; Wright, M.; Upama, M.B.; Chan, K.H.; Xu, C.; Haque, F.; Conibeer, G.; Uddin, A. V_2O_5 -PEDOT: PSS Bilayer as Hole Transport Layer for Highly Efficient and Stable Perovskite Solar Cells. *Org. Electron.* **2018**, *53*, 66–73. [[CrossRef](#)]
14. Choi, S.G.; Seok, H.J.; Rhee, S.; Hahm, D.; Bae, W.K.; Kim, H.K. Magnetron-Sputtered Amorphous V_2O_5 Hole Injection Layer for High Performance Quantum Dot Light-Emitting Diode. *J. Alloys Compd.* **2021**, *878*, 160303. [[CrossRef](#)]
15. Mane, A.A.; Suryawanshi, M.P.; Kim, J.H.; Moholkar, A.V. Fast Response of Sprayed Vanadium Pentoxide (V_2O_5) Nanorods towards Nitrogen Dioxide (NO_2) Gas Detection. *Appl. Surf. Sci.* **2017**, *403*, 540–550. [[CrossRef](#)]
16. Huotari, J.; Bjorklund, R.; Lappalainen, J.; Lloyd Spetz, A. Pulsed Laser Deposited Nanostructured Vanadium Oxide Thin Films Characterized as Ammonia Sensors. *Sens. Actuators B Chem.* **2015**, *217*, 22–29. [[CrossRef](#)]

17. Wang, D.; Gu, K.; Zhao, Q.; Zhai, C.; Yang, T.; Lu, Q.; Zhang, J.; Zhang, M. Synthesis and Trimethylamine Sensing Properties of Spherical V₂O₅ Hierarchical Structures. *New J. Chem.* **2018**, *42*, 14188–14193. [[CrossRef](#)]
18. Jin, W.; Yan, S.; An, L.; Chen, W.; Yang, S.; Zhao, C.; Dai, Y. Enhancement of Ethanol Gas Sensing Response Based on Ordered V₂O₅ Nanowire Microyarns. *Sens. Actuators B Chem.* **2015**, *206*, 284–290. [[CrossRef](#)]
19. Vijayakumar, Y.; Mani, G.K.; Ponnusamy, D.; Shankar, P.; Kulandaisamy, A.J.; Tsuchiya, K.; Rayappan, J.B.B.; Reddy, M.V.R. V₂O₅ Nanofibers: Potential Contestant for High Performance Xylene Sensor. *J. Alloys Compd.* **2018**, *731*, 805–812. [[CrossRef](#)]
20. Nandakumar, N.K.; Seebauer, E.G. Low Temperature Chemical Vapor Deposition of Nanocrystalline V₂O₅ Thin Films. *Thin Solid Film.* **2011**, *519*, 3663–3668. [[CrossRef](#)]
21. Drosos, C.; Jia, C.; Mathew, S.; Palgrave, R.G.; Moss, B.; Kafizas, A.; Vernardou, D. Aerosol-Assisted Chemical Vapor Deposition of V₂O₅ Cathodes with High Rate Capabilities for Magnesium-Ion Batteries. *J. Power Sources* **2018**, *384*, 355–359. [[CrossRef](#)]
22. Hu, B.; Cheng, H.; Huang, C.; Aslam, M.K.; Liu, L.; Xu, C.; Chen, P.; Yu, D.; Chen, C. The Controlled Study of Surfactants on the Morphologies of Three-Dimensional Turbine-like V₂O₅ for the Application of High Performance Lithium Ion Storage. *Solid State Ion.* **2019**, *342*, 115059. [[CrossRef](#)]
23. Margoni, M.M.; Mathuri, S.; Ramamurthi, K.; Babu, R.R.; Ganesh, V.; Sethuraman, K. Hydrothermally Grown Nano and Microstructured V₂O₅ Thin Films for Electrochromic Application. *Appl. Surf. Sci.* **2018**, *449*, 193–202. [[CrossRef](#)]
24. Moretti, A.; Giuli, G.; Trapananti, A.; Passerini, S. Electrochemical and Structural Investigation of Transition Metal Doped V₂O₅ Sono-Aerogel Cathodes for Lithium Metal Batteries. *Solid State Ion.* **2018**, *319*, 46–52. [[CrossRef](#)]
25. Zilberberg, K.; Trost, S.; Meyer, J.; Kahn, A.; Behrendt, A.; Lützenkirchen-Hecht, D.; Frahm, R.; Riedl, T. Inverted Organic Solar Cells with Sol-Gel Processed High Work-Function Vanadium Oxide Hole-Extraction Layers. *Adv. Funct. Mater.* **2011**, *21*, 4776–4783. [[CrossRef](#)]
26. Alsawafta, M.; Almoabadi, A.; Badilescu, S.; Truong, V.-V. Improved Electrochromic Properties of Vanadium Pentoxide Nanorods Prepared by Thermal Treatment of Sol-Gel Dip-Coated Thin Films. *J. Electrochem. Soc.* **2015**, *162*, H466–H472. [[CrossRef](#)]
27. Cholant, C.M.; Westphal, T.M.; Balboni, R.D.C.; Moura, E.A.; Gündel, A.; Flores, W.H.; Pawlicka, A.; Avellaneda, C.O. Thin Films of V₂O₅/MoO₃ and Their Applications in Electrochromism. *J. Solid State Electrochem.* **2017**, *21*, 1509–1515. [[CrossRef](#)]
28. Costa, C.; Pinheiro, C.; Henriques, I.; Laia, C.A.T. Electrochromic Properties of Inkjet Printed Vanadium Oxide Gel on Flexible Polyethylene Terephthalate/Indium Tin Oxide Electrodes. *ACS Appl. Mater. Interfaces* **2012**, *4*, 5266–5275. [[CrossRef](#)] [[PubMed](#)]
29. Gorobtsov, P.Y.; Fisenko, N.A.; Solovey, V.R.; Simonenko, N.P.; Simonenko, E.P.; Volkov, I.A.; Sevastyanov, V.G.; Kuznetsov, N.T. Microstructure and Local Electrophysical Properties of Sol-Gel Derived (In₂O₃-10%SnO₂)/V₂O₅ Films. *Colloids Interface Sci. Commun.* **2021**, *43*, 100452. [[CrossRef](#)]
30. Simonenko, T.L.; Simonenko, N.P.; Gorobtsov, P.Y.; Pozharnitskaya, V.M.; Simonenko, E.P.; Glumov, O.V.; Melnikova, N.A.; Sevastyanov, V.G.; Kuznetsov, N.T. Pen Plotter Printing of MnOx Thin Films Using Manganese Alkoxoacetylacetonate. *Russ. J. Inorg. Chem.* **2021**, *66*, 1416–1424. [[CrossRef](#)]
31. Tamilselvan, M.; Sreekanth, T.V.M.; Yoo, K.; Kim, J. Self-Doped 2D-V₂O₅ Nanoflakes—A High Electrochemical Performance Cathode in Rechargeable Zinc Ion Batteries. *Ceram Int.* **2021**, *47*, 29832–29839. [[CrossRef](#)]
32. Liu, F.; Chen, Z.; Fang, G.; Wang, Z.; Cai, Y.; Tang, B.; Zhou, J.; Liang, S. V₂O₅ Nanospheres with Mixed Vanadium Valences as High Electrochemically Active Aqueous Zinc-Ion Battery Cathode. *Nano-Micro Lett.* **2019**, *11*, 25. [[CrossRef](#)] [[PubMed](#)]
33. Zhang, R.; Qi, L.; Lian, H.; Luo, J. Fabricating Patterned Microstructures by Embedded Droplet Printing on Immiscible Deformable Surfaces. *J. Ind. Eng. Chem.* **2022**, *105*, 138–145. [[CrossRef](#)]
34. Dobrozhan, O.; Baláž, M.; Vorobiov, S.; Baláž, P.; Opanasyuk, A. Morphological, Structural, Optical Properties and Chemical Composition of Flexible Cu₂ZnSnS₄ Thin Films Obtained by Ink-Jet Printing of Polyol-Mediated Nanocrystals. *J. Alloys Compd.* **2020**, *842*, 155883. [[CrossRef](#)]
35. Gorobtsov, P.Y.; Mokrushin, A.S.; Simonenko, T.L.; Simonenko, N.P.; Simonenko, E.P.; Kuznetsov, N.T. Microextrusion Printing of Hierarchically Structured Thick V₂O₅ Film with Independent from Humidity Sensing Response to Benzene. *Materials* **2022**, *15*, 7837. [[CrossRef](#)] [[PubMed](#)]
36. Seo, H.; Iwai, H.; Kishimoto, M.; Ding, C.; Saito, M.; Yoshida, H. Microextrusion Printing for Increasing Electrode–Electrolyte Interface in Anode-Supported Solid Oxide Fuel Cells. *J. Power Sources* **2020**, *450*, 227682. [[CrossRef](#)]
37. Soum, V.; Cheong, H.; Kim, K.; Kim, Y.; Chuong, M.; Ryu, S.R.; Yuen, P.K.; Kwon, O.S.; Shin, K. Programmable Contact Printing Using Ballpoint Pens with a Digital Plotter for Patterning Electrodes on Paper. *ACS Omega* **2018**, *3*, 16866–16873. [[CrossRef](#)]
38. Amin, R.; Ghaderinezhad, F.; Li, L.; Lepowsky, E.; Yenilmez, B.; Knowlton, S.; Tasoglu, S. Continuous-Ink, Multiplexed Pen-Plotter Approach for Low-Cost, High-Throughput Fabrication of Paper-Based Microfluidics. *Anal. Chem.* **2017**, *89*, 6351–6357. [[CrossRef](#)]
39. Simonenko, N.P.; Fisenko, N.A.; Fedorov, F.S.; Simonenko, T.L.; Mokrushin, A.S.; Simonenko, E.P.; Korotcenkov, G.; Sysoev, V.V.; Sevastyanov, V.G.; Kuznetsov, N.T. Printing Technologies as an Emerging Approach in Gas Sensors: Survey of Literature. *Sensors* **2022**, *22*, 3473. [[CrossRef](#)]
40. Yue, Y.; Liang, H. Micro- and Nano-Structured Vanadium Pentoxide (V₂O₅) for Electrodes of Lithium-Ion Batteries. *Adv. Energy Mater.* **2017**, *7*, 1602545. [[CrossRef](#)]
41. Enjalbert, R.; Galy, J. A Refinement of the Structure of V₂O₅. *Acta Crystallogr. Sect. C* **1986**, *42*, 1467–1469. [[CrossRef](#)]
42. Yao, J.; Li, Y.; Massé, R.C.; Uchaker, E.; Cao, G. Revitalized Interest in Vanadium Pentoxide as Cathode Material for Lithium-Ion Batteries and Beyond. *Energy Storage Mater.* **2018**, *11*, 205–259. [[CrossRef](#)]

43. Meyer, J.; Zilberberg, K.; Riedl, T.; Kahn, A. Electronic Structure of Vanadium Pentoxide: An Efficient Hole Injector for Organic Electronic Materials. *J. Appl. Phys.* **2011**, *110*, 033710. [[CrossRef](#)]
44. Shrotriya, V.; Li, G.; Yao, Y.; Chu, C.W.; Yang, Y. Transition Metal Oxides as the Buffer Layer for Polymer Photovoltaic Cells. *Appl. Phys. Lett.* **2006**, *88*, 073508. [[CrossRef](#)]
45. Chiang, W.T.; Su, S.H.; Lin, Y.F.; Yokoyama, M. Increasing the Fill Factor and Power Conversion Efficiency of Polymer Photovoltaic Cell Using $V_2O_5/CuPc$ as a Buffer Layer. *Jpn. J. Appl. Phys.* **2010**, *49*, 04DK14. [[CrossRef](#)]
46. Khan, S.; Singh, K. Influence of Al^{3+} Doping for V^{5+} on the Structural, Optical, Thermal and Electrical Properties of $V_{2-x}Al_xO_{5-\delta}$ ($x=0-0.20$) Ceramics. *Ceram Int.* **2021**, *47*, 10724–10732. [[CrossRef](#)]
47. Sadykov, S.A.; Palchaev, D.K.; Murlieva, Z.K.; Alikhanov, N.M.R.; Rabadanov, M.K.; Gadzhimagomedov, S.K.; Kallaev, S.N. AC Conductivity of $BiFeO_3$ Ceramics Obtained by Spark Plasma Sintering of Nanopowder. *Phys. Solid State* **2017**, *59*, 1771–1777. [[CrossRef](#)]
48. Kang, M.; Jung, J.; Lee, S.Y.; Ryu, J.W.; Kim, S.W. Conductivity, Carrier Density, Mobility, Seebeck Coefficient, and Power Factor in V_2O_5 . *Thermochim. Acta* **2014**, *576*, 71–74. [[CrossRef](#)]
49. Schneider, K.; Dziubaniuk, M.; Wyrwa, J. Impedance Spectroscopy of Vanadium Pentoxide Thin Films. *J. Electron. Mater.* **2019**, *48*, 4085–4091. [[CrossRef](#)]

Disclaimer/Publisher’s Note: The statements, opinions and data contained in all publications are solely those of the individual author(s) and contributor(s) and not of MDPI and/or the editor(s). MDPI and/or the editor(s) disclaim responsibility for any injury to people or property resulting from any ideas, methods, instructions or products referred to in the content.